Summer warmth of the past six interglacials on Greenland

Allison A. Cluett[a,1] and Elizabeth K. Thomas[a]

[a]Department of Geology, State University of New York at Buffalo, Buffalo, NY 14260

Edited by Katherine H. Freeman, Pennsylvania State University, University Park, PA, and approved April 1, 2021 (received for review November 2, 2020)

The relative warmth of mid-to-late Pleistocene interglacials on Greenland has remained unknown, leading to debates about the regional climate forcing that caused past retreat of the Greenland Ice Sheet (GrIS). We analyze the hydrogen isotopic composition of terrestrial biomarkers in Labrador Sea sediments through interglacials of the past 600,000 y to infer millennial-scale summer warmth on southern Greenland. Here, we reconstruct exceptionally warm summers in Marine Isotope Stage (MIS) 5e, concurrent with strong Northern Hemisphere summer insolation. In contrast, "superinterglacial" MIS11 demonstrated only moderate warmth, sustained throughout a prolonged interval of elevated atmospheric carbon dioxide. Strong inferred GrIS retreat during MIS11 relative to MIS5e suggests an indirect relationship between maximum summer temperature and cumulative interglacial mass loss, indicating strong GrIS sensitivity to duration of regional warmth and elevated atmospheric carbon dioxide.

interglacial | Greenland Ice Sheet | Last Interglacial | Arctic | Marine Isotope Stage 11

The Greenland Ice Sheet (GrIS) is projected to contribute between +5 and +33 cm to global sea level by 2100 CE under continued strong anthropogenic forcing (1). Significant uncertainty in projections results, in part, from a lack of constraints on the regional terrestrial climate changes causing past large-scale ice sheet mass loss (2, 3). Extensive retreat of the GrIS likely occurred most recently during Marine Isotope Stage (MIS) 11 (ca. 425 to 375 thousand years before present [ka]), indicated by evidence of coniferous forest cover in southern Greenland coincident with a cessation in the delivery of glacially eroded silts to the Labrador Sea (4, 5) (Figs. 1 and 2). Curiously, Northern Hemisphere summer insolation and atmospheric carbon dioxide (CO_2) forcing were lower during MIS11 than other Pleistocene interglacials through which continental-scale ice persisted on Greenland. For example, the Last Interglacial (MIS5e) (ca. 130 to 115 ka) was associated with stronger Northern Hemisphere summer insolation and briefly higher atmospheric CO_2 concentrations (6, 7). Yet basal sections of seven ice cores contain ice deposited during MIS5e (8), suggesting ice was present on much of the island within this stage.

Sparse paleoclimate evidence suggests that Arctic climate responded nonlinearly to global-scale forcings during past interglacials. For example, MIS11 was one of a few Pleistocene "superinterglacials" identified in the eastern Arctic, with inferred summer air temperatures 4 to 5 °C higher than the current interglacial (MIS1, the Holocene, 11.7 to 0 ka) (9) (Fig. 2*I*). Outstanding Arctic warmth during MIS11 is supported by ostracod assemblages in the Arctic Ocean, indicating summer sea surface temperatures (SSTs) 8 to 10 °C higher than modern (10). Yet regional Arctic temperatures likely differed; summer Labrador SSTs were cooler during MIS11 than MIS1 or MIS5e (4, 11) (Fig. 2*G*). Terrestrial climate on Greenland, where summer air temperature directly influences ice sheet mass balance, remains unconstrained by geologic evidence throughout most Pleistocene interglacials older than MIS5e, including MIS11.

Approach

To evaluate the relative warmth of mid-to-late Pleistocene interglacial summers on southern Greenland, we reconstruct the stable hydrogen isotopic composition (δ^2H) of regional summer precipitation through interglacials from MIS13 to MIS1 using terrestrial biomarkers deposited in marine sediments ~280 km south of Greenland. We use samples from the Ocean Drilling Program Site 646 (58.2093° N, 48.3692° W, and depth 3,460 m) on the northern flank of the Eirik Drift in the Labrador Sea (Fig. 1). The Western Boundary Undercurrent transports sediment to the Eirik Drift from southeastern Greenland and the Denmark Strait, resulting in a dominant southern Greenland source of terrigenous material (4, 12) (See *SI Appendix* for further discussion). In coastal southern Greenland, precipitation δ^2H is primarily determined by the extent of Rayleigh distillation prescribed by cooling during northward moisture transport (13, 14), and ^2H-enrichment of summer precipitation is consistently associated with higher regional atmospheric temperatures on millennial timescales (15) (*SI Appendix*).

Terrestrial Arctic vegetation characteristically synthesizes long-chain (C_{24} to C_{32}) *n*-alkanoic acids, incorporating hydrogen atoms from environmental water and thereby providing a proxy for δ^2H of the source water (16). In coastal Arctic settings, terrestrial vegetation uses growth-season soil water mainly derived from summer-biased precipitation (17). Although pollen-inferred plant communities shifted on southern Greenland during the past six interglacials (4), modern high-latitude shrub tundra and boreal forest taxa demonstrate relatively constant fractionation between

Significance

Recurring glacial retreat and advance eroded most sedimentary records of pre-Holocene interglacials around Greenland, hindering development of long terrestrial paleoclimate records and leading to questions about what climate conditions caused past Greenland Ice Sheet (GrIS) retreat. We infer changes in summer temperature on Greenland from terrestrial biomarkers preserved in marine sediments through the past six interglacials. We find that exceptionally warm summers occurred during MIS5e when the GrIS remained relatively large, in contrast with moderate warmth through MIS11, when the GrIS was likely substantially reduced. Our results suggest that sustained summer warmth, a likely future if anthropogenic carbon emissions are not dramatically reduced, will be more detrimental to future stability of the GrIS than a brief period of exceptional warmth.

Author contributions: A.A.C. and E.K.T. designed research; A.A.C. performed research; A.A.C. and E.K.T. analyzed data; and A.A.C. and E.K.T. wrote the paper.

The authors declare no competing interest.

This article is a PNAS Direct Submission.

[1]To whom correspondence may be addressed. Email: aacluett@buffalo.edu.

This article contains supporting information online at https://www.pnas.org/lookup/suppl/doi:10.1073/pnas.2022916118/-/DCSupplemental.

Published May 10, 2021.

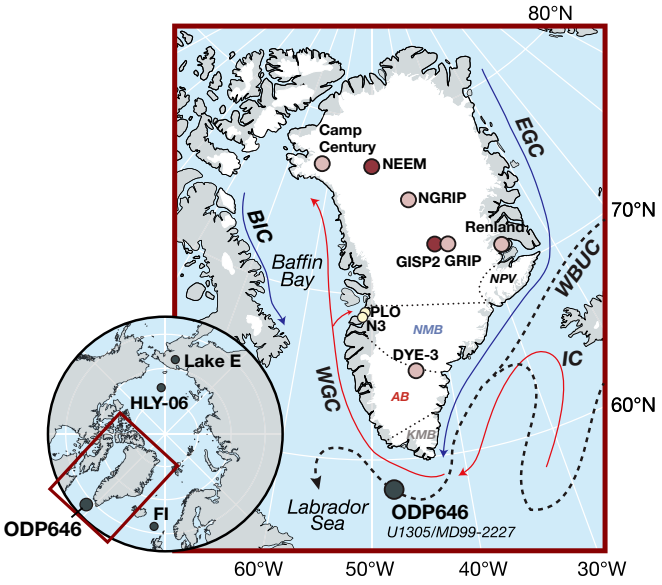

Fig. 1. Map of study region. Location of Eirik Drift core sites (black point), including Ocean Drilling Program Site 646 used in this study. Dotted lines separate silt provenances as in Fig. 2*H* (5, 12). White is the modern glacier extent. Solid lines are the modern schematic surface ocean currents: the West Greenland Current (WGC), Baffin Island Current (BIC), and Irminger Current (IC). The dashed line is the Deep Western Boundary Undercurrent (WBUC). Points are the Greenland ice cores (27), with ice dated to peak (dark red) or late (light red) MIS5e (28–31) and Holocene δ^2H_{C28} records (yellow) (17, 24). The inset map is of Lake El'Gygytgyn (Lake E) (9), Arctic Ocean core HLY-06 (10), and the Faroe Islands (FI) (25).

source water and sedimentary *n*-alkanoic acid δ^2H (18, 19) (*SI Appendix*). Scaling this apparent fractionation based on downcore pollen distributions in Site 646 sediments, a useful though imperfect approach due to differences in transport and preservation between pollen and *n*-alkanoic acids, does not alter the observed patterns of *n*-alkanoic acid δ^2H between or within interglacials in our record (*SI Appendix*, Fig. S1). Therefore, variability in *n*-alkanoic acid δ^2H predominantly reflects variability in summer-biased southern Greenland precipitation δ^2H in this setting. We focus on C_{28} as the longest homolog reliably present in concentrations sufficient for replicate analyses, though δ^2H of C_{24} through C_{30} *n*-alkanoic acids is strongly correlated to δ^2H of the C_{28} homolog (δ^2H_{C28}) in these samples (*SI Appendix*, Fig. S2). Employing an apparent fractionation factor of –93 ± 11‰ (*SI Appendix*), the uppermost sample yields an estimate of precipitation δ^2H of –63 ± 11‰ (*SI Appendix*, Fig. S1), similar to modern monthly summer precipitation δ^2H values (–82 to –67‰) for southernmost Greenland estimated by the Online Isotopes in Precipitation Calculator (20, 21), providing support for the interpretation of δ^2H_{C28} as a signal of summer-biased precipitation δ^2H. However, given the comparatively large uncertainty associated with converting δ^2H_{C28} to absolute precipitation δ^2H relative to our analytical uncertainty, we focus on δ^2H_{C28} values and anomalies rather than absolute precipitation δ^2H values.

Results and Discussion

Interglacial δ^2H_{C28} Trajectories. Site 646 δ^2H_{C28} demonstrates characteristic trajectories through most interglacials (Fig. 2*C*), which are identified based on local planktonic and global benthic foraminiferal stable oxygen isotopic compositions ($\delta^{18}O$) (Fig. 2*E*) (4, 22). δ^2H_{C28} generally increases steeply through glacial terminations, achieves brief early maxima occasionally followed by an interval of stability, and slowly declines through subsequent glacial inceptions. Because proximal production of long-chain *n*-alkanoic acids requires an ice-free vegetated Greenland margin, Site 646 δ^2H_{C28} should not capture the earliest stages of glacial terminations, given the full glacial extent of the GrIS to the continental shelf (23). δ^2H_{C28} values in glacial-age sediments suggest remobilization of interglacial-aged organic material stored on the landscape during periods of GrIS advance (*SI Appendix*, Fig. S3).

Corroboration by Regional Climate Records during MIS1 and MIS5e. Terrestrial Arctic climate is well constrained through MIS1, and comparison to other proxy records spanning this stage supports the fidelity of Site 646 δ^2H_{C28} to record regional interglacial climate. Throughout MIS1, δ^2H_{C28} declined by 28‰, in close agreement with coastal summer-biased δ^2H_{C28} records from western Greenland and the Faroe Islands (Fig. 3*C*) (17, 24, 25). Inferred trends in precipitation δ^2H are congruent with regional temperatures, which exhibited an early MIS1 maximum in phase with Northern Hemisphere summer insolation (Fig. 3 *A* and *F*) (6, 26) but contrasted with persistently low reconstructed Labrador SSTs (Fig. 2*G*) (4). Southern and eastern Greenland ice core $\delta^{18}O$ demonstrate either early MIS1 maxima or stable values following the Last Termination, with early MIS1 warmth masked by elevation changes in some records (Fig. 3*E*) (27).

During MIS5e, Site 646 δ^2H_{C28} is further corroborated by basal ice core sections, which reveal a strong precipitation isotope response on Greenland (Figs. 1 and 3*E*). δ^2H_{C28} reached a maximum 36‰ above the last millennium, comparable to North Greenland Eemian Ice Drilling Project (NEEM) and Greenland Ice Sheet Project 2 (GISP2) ice cores which, respectively, had peak MIS5e $\delta^{18}O$ anomalies of +2.6‰ and +3.6‰ (~+21‰ and +29‰ δ^2H) (28, 29). Additional sequences extending only into late MIS5e from North Greenland Ice Core Project (NGRIP), Greenland Ice Core Project (GRIP), Camp Century, and Renland ice cores record $\delta^{18}O$ anomalies of +2.2 to +3.7‰ (~+18 to +30‰ δ^2H) (30, 31). Strongly enriched precipitation isotope signals in Greenland contrast with a muted response in late MIS5e in the Faroe Islands (25), implying regional North Atlantic variability. Changes in sea ice extent and/or precipitation seasonality are necessary to explain the magnitude of the annual ice core isotopic signals observed during MIS5e (15). Here, however, we infer a signal of similar magnitude in summer-biased precipitation, suggesting particularly high regional summer temperatures, which are directly relevant to ice sheet mass balance.

Spatial Variability of Arctic Interglacials. Among analyzed interglacials at Site 646, MIS1, MIS5e, and MIS11 demonstrate the most enriched δ^2H_{C28} of the past 600 ka (Fig. 4*A*), with values greater than –130‰ persisting for more than 10 thousand y (kyr) during MIS5e and MIS11 (Figs. 2*C* and 3*C*). The maximum δ^2H_{C28} value during MIS11 was ca. 10‰ lower than MIS5e, indicating slightly lower summer temperatures in southern Greenland during MIS11 than MIS5e. Comparison of δ^2H_{C28} data with Site 646 pollen suggests conditions may have been warm enough to support local spruce on southern Greenland during other interglacials, but local colonization was only achieved during the exceptionally long MIS11 (Fig. 2*J*) (4). The pattern of moderate but not exceptional warmth on Greenland during MIS11 relative to MIS5e agrees with transient ice-climate simulations (32), Labrador SSTs (4, 11), and a global synthesis of relative interglacial intensity (33). However, moderate summer temperatures in southern Greenland and the Labrador Sea during MIS11 contrast with Siberian and Arctic Ocean records indicating exceptionally warm conditions (9, 10) (Figs. 1 and 2*I*), providing evidence for broad regional Arctic climate variability throughout this stage, despite equivalent insolation and CO_2 forcing across Northern Hemisphere high latitudes.

Periods of sustained enriched δ^2H_{C28} in MIS11 and MIS5e coincide with persistent strong North Atlantic Deepwater (NADW)

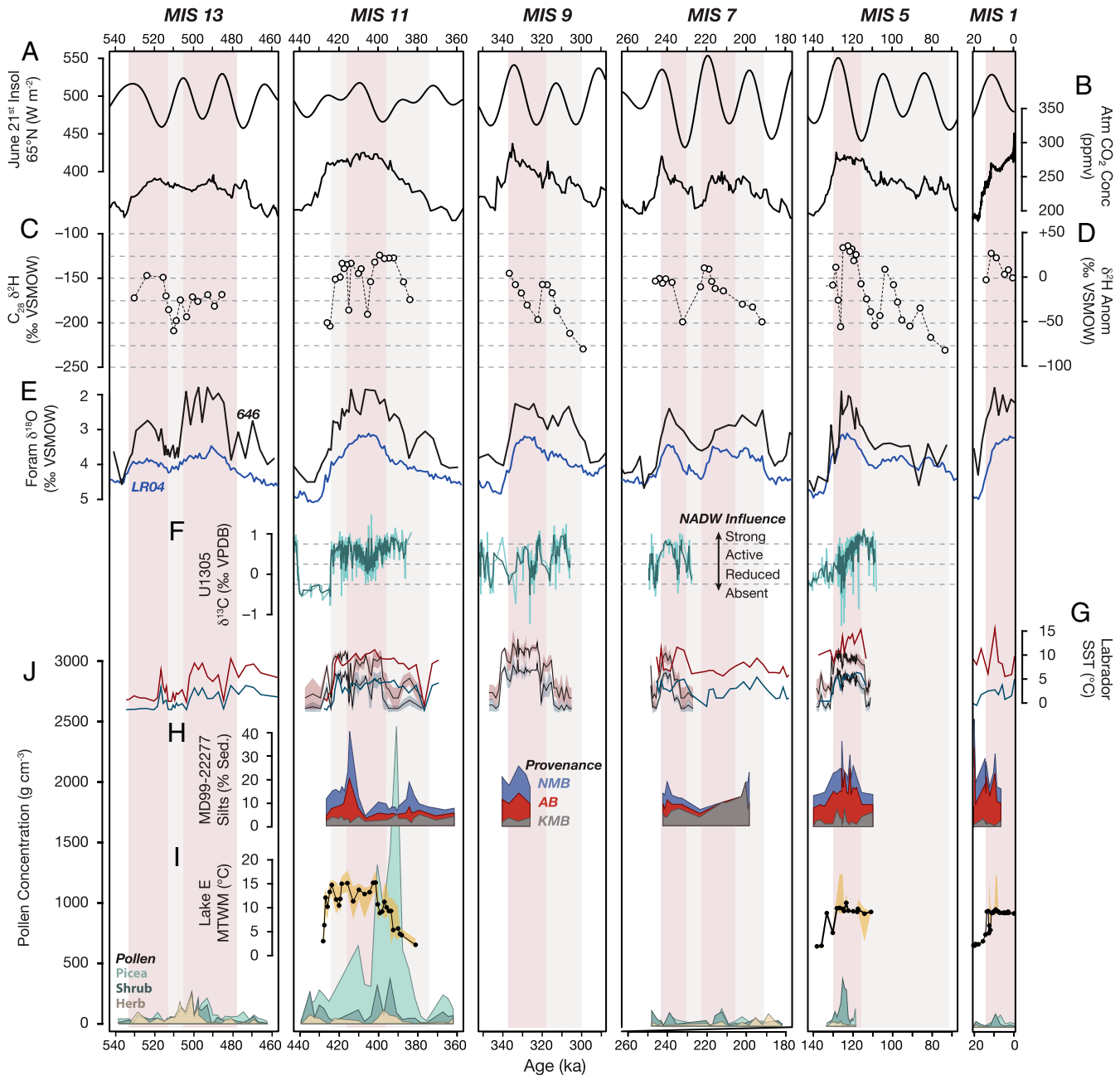

Fig. 2. Interglacial records from MIS13 to MIS1. Datasets are plotted on their own age scales and not synchronized, except those from the same sites. Formally defined MIS and peak substage (22) (as in Fig. 4) are shaded. (*A*) June 21st insolation at 65°N (6). (*B*) Atmospheric CO_2 concentration (7). (*C*) Site 646 δ^2H_{C28} (this study). Analytical error is smaller than point size (*SI Appendix*). (*D*) Site 646 δ^2H_{C28} as an anomaly relative to the last millennium. (*E*) Global benthic (blue) and Site 646 planktic foraminifera $\delta^{18}O$ (black) (4, 22). (*F*) Stable carbon isotopes ($\delta^{13}C$, ‰ VPDB [Vienna Pee Dee Belemnite]) of *Cibicidoides wuellerstorfi* from U1305 (34). (*G*) SSTs from U1305 (summer: black and red error envelope; winter: black and blue error envelope) (11) and Site 646 (summer: red; winter: blue) (4). (*H*) Provenance of MD99-2227 silts as in Fig. 1 (5, 12). (*I*) Mean temperature of the warmest month (MTWM) from Lake El'Gygytgyn (9). (*J*) Site 646 pollen concentrations (4).

formation, linking stable North Atlantic climate and deep-ocean circulation at millennial scales during relatively warm interglacials (Fig. 2*F*) (34). In contrast, MIS9 and MIS7 exhibit instability in both δ^2H_{C28} and NADW formation, suggesting a lack of establishment of stable North Atlantic heat transport during these stages. Yet even during the early intervals of MIS5e and MIS11, vigorous NADW formation was likely perturbed by freshwater fluxes associated with the decay of Northern Hemisphere ice sheets, punctuating stable warmth with centennial-to-millennial–scale cooling (34). δ^2H_{C28} yields evidence for such instabilities ca. 410 and 130 ka, albeit at low resolution. Furthermore, a lack of expression of "superinterglacial" warmth in the North Atlantic sector during MIS11 supports previous interpretations that exceptionally warm conditions in the eastern Arctic were not caused by enhanced North Atlantic heat transport but rather by the reduction of North Pacific upwelling due to reduced Antarctic Bottom Water formation caused by West Antarctic Ice Sheet collapse (9, 35).

Implications for Climate–Ice Sheet Sensitivity. Although Site 646 δ^2H_{C28} provides evidence that Southern Greenland summer temperatures were not outstanding during MIS11 within the

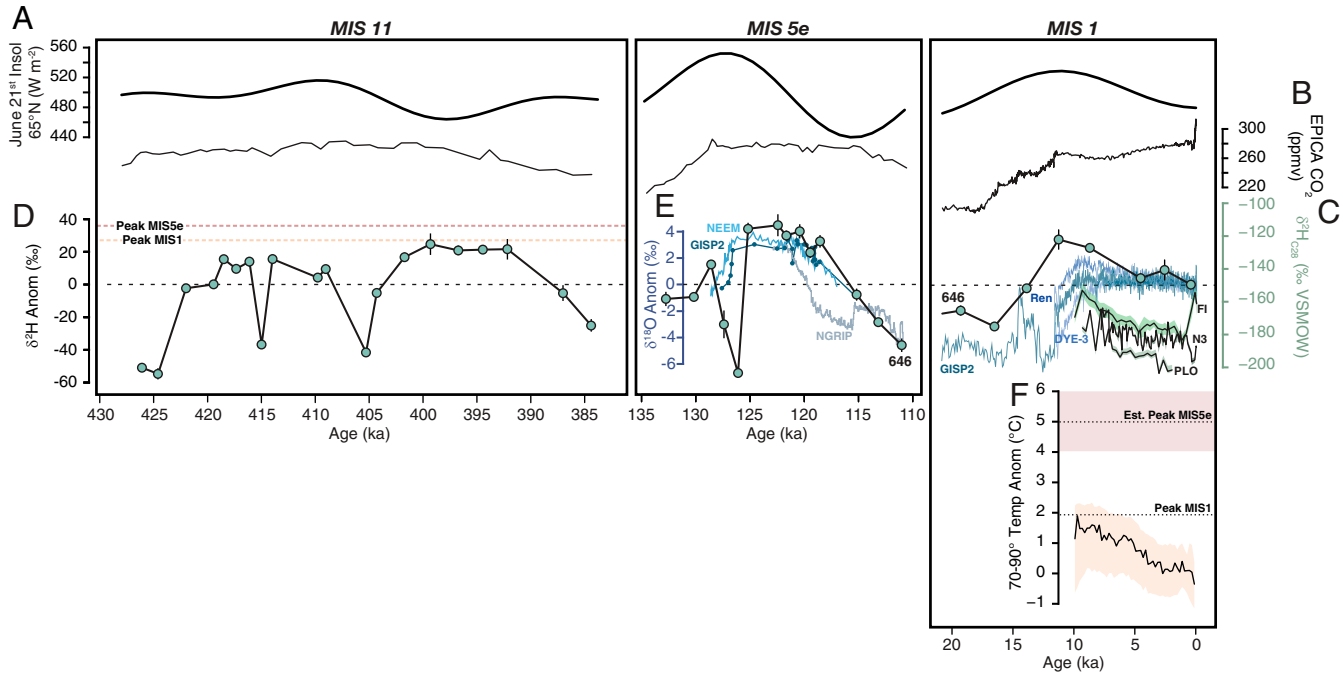

Fig. 3. Comparison of paleoclimate constraints from MIS1, MIS5e, and MIS11, contextualized by insolation (*A*) (6) and atmospheric CO_2 (*B*) (7) forcings. δ^2H_{C28} from this study (646) is plotted as absolute values in comparison to absolute values of western Greenland (N3, Pluto [PLO]) and Faroe Island (FI) lake sediment δ^2H_{C28} from MIS1 (*C*, right-hand *y*-axis in green) (17, 24, 25). Site 646 δ^2H_{C28} is additionally presented as an anomaly relative to the last millennium (*D*, left-hand *y*-axis in black) for comparison to Greenland ice core $\delta^{18}O$ anomalies (*y*-axis in blue) through MIS1 and MIS5e (*E*) (27–31). Southern and eastern Greenland ice core $\delta^{18}O$ records are plotted in MIS1, whereas all Greenland ice cores with semicontinuous sequences are included in MIS5e. The ice core $\delta^{18}O$ axis is scaled by eight times for comparison to δ^2H. Isotope records are compared to a synthesis of Arctic summer temperature (26) and estimated peak Arctic MIS5e temperature (43) (*F*).

context of the past 600 ka, MIS11 ^2H-enrichment exceeded the magnitude expected from insolation forcing alone (Fig. 4) (6). For most interglacials in our record, highest δ^2H_{C28} occurred following glacial terminations, in phase with approximately covarying Northern Hemisphere summer insolation and CO_2 (Fig. 2 *A*–*C*). In contrast, maximum MIS11 δ^2H_{C28} occurred midstage, when elevated CO_2 diverged from distinctively low insolation (Fig. 3). Though the causes of CO_2 concentrations within mid-to-late Pleistocene interglacials remain poorly understood (33), the decoupling of insolation and CO_2 during MIS11 suggests that this stage may be a particularly useful analog for the evaluation of GrIS sensitivity to anthropogenic carbon emissions.

Comparison of southern Greenland δ^2H_{C28} to constraints on past GrIS behavior suggests an indirect relationship between maximum regional summer temperatures and cumulative interglacial GrIS mass loss. Strong inferred GrIS retreat during MIS11 occurred in response to moderate summer warmth sustained for over 10 ka, rather than exceptionally high but comparatively brief summer warmth, as in MIS5e when the GrIS remained relatively extensive (Fig. 3). Proxy data and ice sheet model simulations suggest continued retreat for ca. 16 kyr in MIS11 throughout the duration of stable warmth (5, 12, 32). Likewise, Site 646 sedimentary spruce pollen concentrations indicate forest expansion throughout the interval of stable MIS11 warmth, until both pollen concentrations and δ^2H_{C28} declined ca. 390 ka, indicating the onset of ice sheet expansion and cooler summers (Fig. 2*J*) (4). Lower eccentricity and obliquity of the MIS11 orbital configuration meant that summers, though less intense, were longer than during MIS5e (6), which in conjunction with high CO_2, would have favored longer melt and growing seasons during the prolonged warmth of this stage.

Here, δ^2H_{C28} provides direct evidence to support the hypothesis that the millennial-scale duration of elevated terrestrial interglacial warmth, rather than maximum summer temperature, is the predominant control on orbital-scale GrIS stability (5, 11, 32). Given the similar orbital configuration today to during MIS11 (6), sustained elevated summer temperatures associated with persistently high atmospheric CO_2 concentrations, a probable future if anthropogenic greenhouse gas emissions are not dramatically reduced (36), will likely be more detrimental to the future long-term stability of the GrIS than a brief overshoot of exceptional summer temperature.

Materials and Methods

Chronology and Sampling. Sediment samples were selected from the aligned composite sequence of cores from Holes 646A and 646B (4). Selected samples span the past ca. 550,000 y at relatively high resolution throughout interglacial periods and lower resolution throughout glacial periods. Data are presented on a revised mid-to-late Pleistocene age-depth model (CT20), based on that presented by de Vernal and Hillaire-Marcel (DH08) (*SI Appendix*, Fig. S4) (4). The chronology is developed by correlating *Neogloboquadrina pachyderma* (left coiled) $\delta^{18}O$ reported by Aksu and Hillaire-Marcel (37) to the global benthic foraminifera $\delta^{18}O$ stack (LR04) (22), with additional comparison to *N. pachyderma* $\delta^{18}O$ from the Eirik Drift core MD99-2227 (58.21°N, 48.37°W, and 3,460 m depth) (38). Age–model correlation was performed in Analyseries (39), and sample ages were linearly interpolated at the median composite sample depth from scaled $\delta^{18}O$ ages. Because of dating uncertainty, we do not specifically comment on the timing of the onset or peak warmth in our record. However, we note that all data from the 646 cores (i.e., pollen concentrations, dinocyst-inferred SSTs, planktic foraminifera $\delta^{18}O$, and δ^2H_{C28}) are presented on the revised age scale (Fig. 2), and comparisons of timing among these datasets are robust. Samples are assigned to MISs as formally defined, based on the LR04 stack and substages according to the framework of Railsback, Gibbard, Head, Voarintsoa, and Toucanne (40).

***N*-Alkanoic Acid Extraction and Purification.** *N*-alkanoic acids were extracted, purified, and analyzed in the University at Buffalo Organic and Stable Isotope Biogeochemistry Laboratory following the procedures published by Thomas, Hollister, Cluett, and Corcoran (17). We freeze-dried bulk sediment

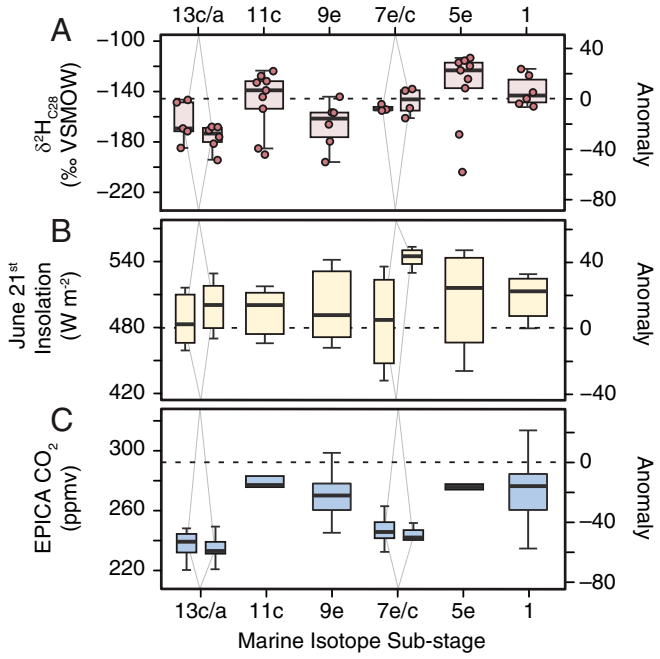

Fig. 4. Climate forcings and southern Greenland response during peak Marine Isotope substages. Both substages were included for MIS13 and MIS7, when peak substages are poorly defined. Comparison of δ^2H_{C28} (*A*), 65°N insolation (*B*) (6), and CO_2 (*C*) (7) between peak Marine Isotope substages. Boxplots represent distribution of values within the substage. Dashed lines indicate the mean for 1 to 0 ka, and right axes present values as anomalies relative to this mean.

samples and homogenized sediments with a mortar and pestle. We extracted lipids from homogenized bulk sediments mixed with ~1/3 diatomaceous earth by volume using an Accelerated Solvent Extractor (Dionex ASE-200) using methylene chloride (DCM):methanol 9:1 (volume:volume [*v*:*v*]), heated to 120 °C at 1,200 psi for 10 min three times. We added a cis-eicosenoic acid internal standard to extracted lipids and then separated the acid fraction from the total lipid extract using flash columns with an aminopropyl silica gel solid phase. We collected the neutral fraction first in DCM:isopropanol 2:1 (*v*:*v*), followed by the acid fraction in 4% acetic acid in DCM. We methylated the acid fraction in acidified methanol at 60 °C for 8 h, converting fatty acids into fatty acid methyl esters (FAMEs). We extracted FAMEs in hexane three times from a hexane-saltwater mixture and performed a final cleanup of FAMEs with a flash column silica gel solid phase, collecting FAMEs in DCM following elution of apolar compounds in hexane. All flash columns used three column volumes of each eluent.

Analytical Methods. We quantified the relative abundance of *n*-alkanoic acids on a Thermo Trace 1310 Gas Chromatograph (GC) with a flame ionization detector. FAMEs were injected on a split/splitless inlet held at 250 °C run in splitless mode for the first 0.75 min with a split flow of 14 mL/min thereafter. Column flow was constant at 3.6 mL/min using hydrogen carrier gas. Oven temperature started at 70 °C, held for 1 min, then ramped at 27 °C/min to 230 °C, and followed immediately by a ramp of 6 °C/min to 315 °C, with a final hold of 10 min. All analyses used HP-1ms columns (Agilent) with a length of 30 m, inner diameter of 0.25 mm, and film thickness of 0.25 μm. Relatively high concentrations of mono- and diunsaturated *n*-alkanoic acids were observed in a subset of samples (*SI Appendix*, Fig. S5). To minimize the potential impact of coelution of these unsaturated *n*-alkanoic acids on measured saturated *n*-alkanoic acid δ^2H values, samples for which the ratio of the sum of mono- and diunsaturated C_{28} *n*-alkanoic acids to saturated C_{28} *n*-alkanoic acids is greater than 0.20 were flagged and excluded from analysis.

We measured FAME δ^2H values on a Thermo Delta V Plus isotope ratio mass spectrometer (IRMS) coupled to a Thermo Trace 1310 GC with a GC-Isolink II and a Conflo IV. GC-IRMS analyses followed the same GC methods as quantification using the same column, with the substitution of helium carrier gas at a constant flow of 1.5 mL/min. *N*-alkanoic acids were converted to H_2 gas in a pyrolysis reactor held at 1,420 °C. A total of 88 of the 143 successfully measured samples were injected in triplicate, while 24 samples were injected in duplicate and 31 just once because of the low abundance of *n*-alkanoic acids. For each run, a suite of standards with known isotopic composition (A. Schimmelmann, Indiana University, Bloomington, IN) was included to check for instrument drift (C_{18} and C_{24} FAMEs) and peak-size linearity (C_{20} and C_{28} FAMEs) and to normalize measured values to Vienna Standard Mean Ocean Water. We corrected for the isotopic value of the hydrogens added during methylation. Methyl group hydrogen δ^2H was determined based on methylation of phthalic acid with known isotopic composition (41). Total random and analytical uncertainty expressed as the SEM averaged 3.2‰ for C_{28}. The H^{3+} factor was determined at the start of each sequence and was 2.47 ± 0.47 to 4.65 ± 0.29 throughout, with a mean of 3.43 ± 0.41.

Data Availability. Data are available in the National Oceanic and Atmospheric Administration (NOAA) Paleoclimatology database. Leaf wax δ^2H and concentrations data have been deposited in the NOAA Paleoclimatology Database (https://www.ncdc.noaa.gov/paleo/study/30412) (42). All other study data are included in the article and/or *SI Appendix*.

ACKNOWLEDGMENTS. We thank K. Lovell, M. Prabhakar, O. Cowling, and K. Hollister for assistance processing samples and J. Briner for providing feedback on the manuscript. We thank R. Hatfield and A. Reyes for sharing data from core MD99-2227 and the two anonymous reviewers for providing constructive feedback. This study was funded by a US Science Support Program Schlanger Fellowship to A.A.C., NSF Graduate Research Fellowship No. 1645677 to A.A.C., and NSF Division of Earth Sciences Instrumentation and Facilities grant 1652274 to E.K.T.

1. A. Aschwanden *et al.*, Contribution of the Greenland Ice Sheet to sea level over the next millennium. *Sci. Adv.* **5**, eaav9396 (2019).
2. B. L. Otto-Bliesner *et al.*, The PMIP4 contribution to CMIP6–Part 2: Two interglacials, scientific objective and experimental design for Holocene and Last Interglacial simulations. *Geosci. Model Dev.* **10**, 3979–4003 (2017).
3. J. P. Briner *et al.*, Rate of mass loss from the Greenland Ice Sheet will exceed Holocene values this century. *Nature* **586**, 70–74 (2020).
4. A. de Vernal, C. Hillaire-Marcel, Natural variability of Greenland climate, vegetation, and ice volume during the past million years. *Science* **320**, 1622–1625 (2008).
5. A. V. Reyes *et al.*, South Greenland ice-sheet collapse during Marine Isotope Stage 11. *Nature* **510**, 525–528 (2014).
6. J. Laskar *et al.*, A long-term numerical solution for the insolation quantities of the Earth. *Astron. Astrophys.* **428**, 261–285 (2004).
7. B. Bereiter *et al.*, Revision of the EPICA Dome C CO2 record from 800 to 600 kyr before present. *Geophys. Res. Lett.* **42**, 542–549 (2015).
8. A. Landais *et al.*, How warm was Greenland during the last interglacial period? *Clim. Past* **12**, 1933–1948 (2016).
9. M. Melles *et al.*, 2.8 million years of Arctic climate change from Lake El'gygytgyn, NE Russia. *Science* **337**, 315–320 (2012).
10. T. M. Cronin *et al.*, A 600-ka Arctic sea-ice record from Mendeleev Ridge based on ostracodes. *Quat. Sci. Rev.* **79**, 157–167 (2013).
11. N. Irvalı *et al.*, A low climate threshold for south Greenland Ice Sheet demise during the Late Pleistocene. *Proc. Natl. Acad. Sci. U.S.A.* **117**, 190–195 (2020).
12. R. G. Hatfield *et al.*, Interglacial responses of the southern Greenland ice sheet over the last 430,000 years determined using particle-size specific magnetic and isotopic tracers. *Earth Planet. Sci. Lett.* **454**, 225–236 (2016).
13. J. Nusbaumer, P. M. Alexander, A. N. LeGrande, M. Tedesco, Spatial shift of Greenland moisture sources related to enhanced Arctic warming. *Geophys. Res. Lett.* **46**, 14723–14731 (2019).
14. J.-L. Bonne *et al.*, The isotopic composition of water vapour and precipitation in Ivittuut, southern Greenland. *Atmos. Chem. Phys.* **14**, 4419–4439 (2014).
15. P. Gierz, M. Werner, G. Lohmann, Simulating climate and stable water isotopes during the Last Interglacial using a coupled climate-isotope model. *J. Adv. Model. Earth Syst.* **9**, 2027–2045 (2017).
16. W. C. Daniels *et al.*, Hydrogen isotope fractionation in leaf waxes in the Alaskan Arctic tundra. *Geochim. Cosmochim. Acta* **213**, 216–236 (2017).
17. E. K. Thomas, K. V. Hollister, A. A. Cluett, M. C. Corcoran, Reconstructing Arctic precipitation seasonality using aquatic leaf wax δ2H in lakes with contrasting residence times. *Paleoceanograp. Paleoclimatol.* **35**, e2020PA003886 (2020).
18. J. M. McFarlin, Y. Axford, A. L. Masterson, M. R. Osburn, Calibration of modern sedimentary δ^2H plant wax-water relationships in Greenland lakes. *Quat. Sci. Rev.* **225**, 105978 (2019).
19. A. Bakkelund, T. J. Porter, D. G. Froese, S. J. Feakins, Net fractionation of hydrogen isotopes in *n*-alkanoic acids from soils in the northern boreal forest. *Org. Geochem.* **125**, 1–13 (2018).
20. G. J. Bowen, The Online Isotopes in Precipitation Calculator, Version 3.1. https://wateriso.utah.edu/waterisotopes/index.html. (2021). Accessed 16 February 2021.

21. G. J. Bowen, L. I. Wassenaar, K. A. Hobson, Global application of stable hydrogen and oxygen isotopes to wildlife forensics. *Oecologia* **143**, 337–348 (2005).
22. L. E. Lisiecki, M. E. Raymo, A Pliocene-Pleistocene stack of 57 globally distributed benthic δ^{18}O records. Paleoceanograp. Paleoclimatol 20, PA1003 (2005).Correction in: Paleoceanograp. Paleoclimatol 20 (2005).
23. L. Håkansson, J. Briner, H. Alexanderson, A. Aldahan, G. Possnert, ^{10}Be ages from central east Greenland constrain the extent of the Greenland ice sheet during the Last Glacial Maximum. *Quat. Sci. Rev.* **26**, 2316–2321 (2007).
24. E. K. Thomas, J. P. Briner, J. J. Ryan-Henry, Y. Huang, A major increase in winter snowfall during the middle Holocene on western Greenland caused by reduced sea ice in Baffin Bay and the Labrador Sea. *Geophys. Res. Lett.* **43**, 5302–5308 (2016).
25. L. Curtin *et al*., Holocene and Last Interglacial climate of the Faroe Islands from sedimentary plant wax hydrogen and carbon isotopes. *Quat. Sci. Rev.* **223**, 105930 (2019).
26. C. C. Routson *et al*., Mid-latitude net precipitation decreased with Arctic warming during the Holocene. *Nature* **568**, 83–87 (2019).
27. B. M. Vinther *et al*., Holocene thinning of the Greenland ice sheet. *Nature* **461**, 385–388 (2009).
28. NEEM community members, Eemian interglacial reconstructed from a Greenland folded ice core. *Nature* **493**, 489–494 (2013).
29. A. M. Yau, M. L. Bender, A. Robinson, E. J. Brook, Reconstructing the last interglacial at Summit, Greenland: Insights from GISP2. *Proc. Natl. Acad. Sci. U.S.A.* **113**, 9710–9715 (2016).
30. S. J. Johnsen *et al*., Oxygen isotope and palaeotemperature records from six Greenland ice-core stations: Camp Century, Dye-3, GRIP, GISP2, Renland and NorthGRIP. *J. Quaternary Sci.* **16**, 299–307 (2001).
31. P. Kindler *et al*., Temperature reconstruction from 10 to 120 kyr b2k from the NGRIP ice core. *Clim. Past* **10**, 887–902 (2014).
32. A. Robinson, J. Alvarez-Solas, R. Calov, A. Ganopolski, M. Montoya, MIS-11 duration key to disappearance of the Greenland ice sheet. *Nat. Commun.* **8**, 16008 (2017).
33. PAGES, Interglacials of the last 800,000 years. *Rev. Geophys.* **54**, 162–219 (2016).
34. E. V. Galaasen *et al*., Interglacial instability of North Atlantic deep water ventilation. *Science* **367**, 1485–1489 (2020).
35. A. J. Coletti, R. M. DeConto, J. Brigham-Grette, M. Melles, A GCM comparison of Pleistocene super-interglacial periods in relation to Lake El'gygytgyn, NE Arctic Russia. *Clim. Past* **11**, 979–989 (2015).
36. P. U. Clark *et al*., Consequences of twenty-first-century policy for multi-millennial climate and sea-level change. *Nat. Clim. Chang.* **6**, 360–369 (2016).
37. A. E. Aksu, C. Hillaire-Marcel, "Upper Miocene to Holocene oxygen and carbon isotopic stratigraphy of Sites 646 and 647, Labrador Sea" in *Proceedings of ODP. Sci. Results*, S. P. Srivastava *et al*., Eds. (Ocean Drilling Program, College Station, TX 1989), vol. 105, pp. 689–704.
38. H. F. Evans *et al*., Paleointensity-assisted chronostratigraphy of detrital layers on the Eirik Drift (North Atlantic) since marine isotope stage 11. *Geochem. Geophys. Geosyst.* **8** Q11007 (2007).
39. D. L. Paillard, L. Labeyrie, P. Yiou, Macintosh program performs time-series analysis. *Eos (Wash. D.C.)* **77**, 379 (1996).
40. L. B. Railsback, P. L. Gibbard, M. J. Head, N. R. G. Voarintsoa, S. Toucanne, An optimized scheme of lettered marine isotope substages for the last 1.0 million years, and the climatostratigraphic nature of isotope stages and substages. *Quat. Sci. Rev.* **111**, 94–106 (2015).
41. H. Lee *et al*., Comparison of three methods for the methylation of aliphatic and aromatic compounds. *Rapid Commun. Mass Spectrom.* **31**, 1633–1640 (2017).
42. A. A. Cluett, E. K. Thomas, ODP 646 Interglacial Leaf Wax δ2H. NOAA Paleoclimatology Database. https://www.ncdc.noaa.gov/paleo/study/30412. Deposited 8 July 2020.
43. CAPE-Last Interglacial Project Members, Last Interglacial Arctic warmth confirms polar amplification of climate change. *Quat. Sci. Rev.* **25**, 1383–1400 (2006).